SUPPLEMENTARY INFORMATION

Smart Resonant Micro-sensor and Micro-actuator: High-Performance, Wide Range Bi-Axial Magnetic Sensitive/ Insensitive Micro-Device for Multifunctional Sensing Applications

Hanin Amara[1], Nadeem Tariq Beigh[1], and Nouha Alcheikh[1*]

[1]Department of Mechanical and Nuclear Engineering, Khalifa University, Abu Dhabi, 127788, United Arab Emirates

*****_Corresponding author:_ nouha.alcheikh@ku.ac.ae

Table of Contents:

Supplementary Section 1: Geometrical parameters

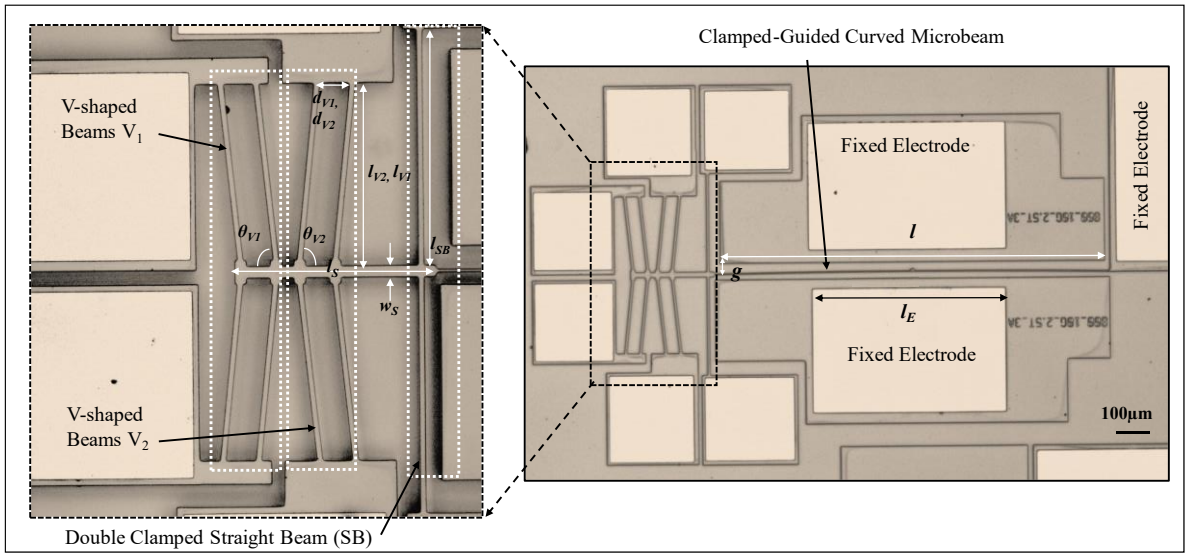

Fig. S1. The fabricated microresonator highlights the three actuators: V-shaped beams V_1, V_2, and double-clamped straight beams (SB), fixed electrodes, and clamp-guided curved microbeam.

Table S1. Main geometric parameters of the designed microresonator

Components	Geometric parameters	Value
Microbeam	Length l	1000 µm
	Width w	2.5 µm
	Thickness h	25 µm
	Initial Rise b_o	3 µm
Driving electrode	Length l_E	-
	Air gap g	10 µm
Actuator V_1	Length l_{V1}	150 µm
	Theta θ_{V1}	5°
	Gap d_{V1}	27 µm
	Width w_{V1}	5 µm
Actuator V_2	Length l_{V2}	150 µm
	Theta θ_{V2}	5°
	Gap d_{V2}	27 µm
	Width w_{V2}	5 µm
Actuator SB	Length l_{SB}	200 µm
	Width w_{SB}	5 µm
Shuttle	Length l_S	175 µm
	Width w_S	10.5 µm

Supplementary Section 2: Fabrication Process

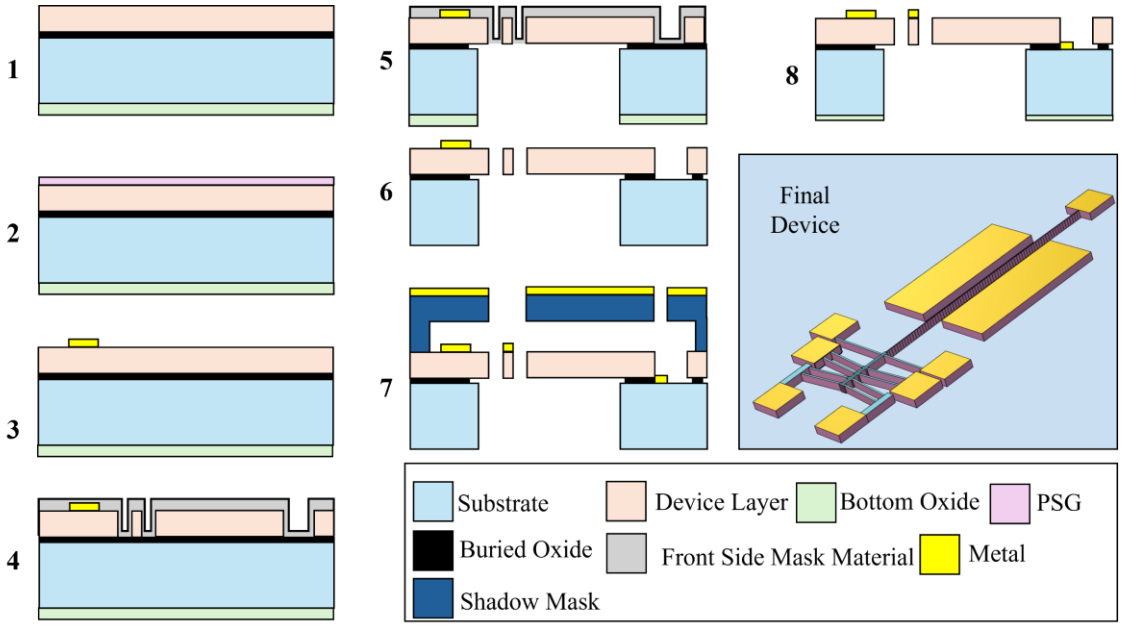

Fig. S2. SOIMUMPS process flow.

The SOIMUMPs process is a straightforward four-mask SOI patterning and etching method developed from research conducted at MEMSCAP (formerly known as Cronos Integrated Microsystems and the MCNC MEMS Technology Applications Center). This process flow was initially created to fabricate MEMS variable optical attenuator (VOA) devices based on patented thermal actuator technology.

The process begins with 100 mm n-type double-side polished silicon on insulator (SOI) wafers. These wafers consist of either a 10 µm or a 25 µm silicon layer, a 1 µm oxide layer, and a 400 µm substrate layer. A thinner bottom-side oxide layer is also beneath the substrate layer (Figure S2(1)). The top surface of the silicon layer is doped by depositing a phosphor-silicate glass (PSG) layer and annealing it at 1050°C for one hour in an argon atmosphere (Figure S2(2)). This PSG layer is then removed using wet chemical etching.

The first step in the process involves applying the pad metal (Figure S2(3)). A metal stack made up from 20 nm of chrome and 500 nm of gold is patterned through a liftoff technique (Lines with a width of three µm and a 3 µm space can be patterned with a 3 µm alignment tolerance to the device layer). This metal area must be covered during the subsequent deep reactive ion etching (DRIE). Consequently, it is limited to large areas within the actuator.

Next, Silicon is lithographically patterned using the second mask level, and a deep reactive ion etch (DRIE) is performed. This etch utilizes inductively coupled plasma (ICP) technology, employing a specific SOI recipe designed to minimize undercutting of the silicon layer when the etch reaches the oxide. Further,

frontside protection material is applied to the top surface of the silicon layer (Figure S2(4)). The wafers are then flipped over, and the substrate layer is lithographically patterned from the bottom side using the third mask level, referred to as TRENCH. This pattern is then reactive ion etched (RIE) into the bottom-side oxide layer. A DRIE silicon etch is used afterward to etch these features completely through the substrate layer (Figure S2(5)). Following this, a wet oxide etch process is employed to remove the oxide layer in regions defined by the TRENCH mask (Figure S2(6)). The frontside protection material is subsequently stripped away using a dry etch process, which “releases” any mechanical structures in the silicon layer that are situated over the through-holes defined in the substrate layer. Any remaining exposed oxide layer is removed from the wafers using a vapor HF process to minimize stiction. This oxide layer is eliminated to facilitate electrical contact with the substrate and to create an undercut in the oxide layer, which helps prevent metal shorts between the silicon layer and the substrate layer.

Finally, a blanket metal layer, consisting of 50 nm of chromium and 600 nm of gold, is deposited, and patterned using a shadow masking technique (Figure S2(7)). The shadow mask is prepared from a separate double-side polished silicon wafer. "Standoffs" are included on the side of the shadow mask that will contact the SOI wafer to prevent any interference with the patterned features in the silicon layer. The shadow mask is then patterned with the METAL mask, and through-holes are etched using DRIE. The shadow mask is aligned and temporarily bonded to the SOI wafer, after which the metal is e-beam evaporated. This metal is deposited on the top surface of the silicon layer only in the regions corresponding to the through-holes in the shadow mask. Once the evaporation process is complete, the shadow mask is removed, leaving a patterned metal layer on the SOI wafer (Figure S2(8)). Therefore, completing the device fabrication (Final Device).

Supplementary Section 3: Experimental Setup

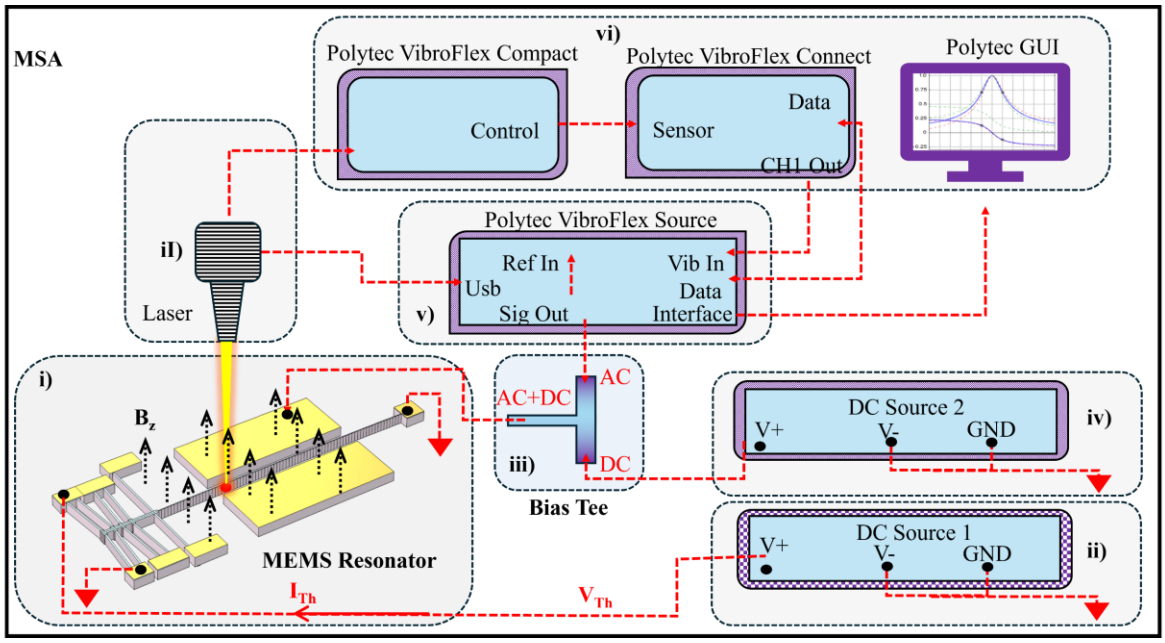

Fig. S3. The experimental setup.

The MEMS magnetometer characterization setup is shown in Figure S3. Firstly, the MEMS resonator is positioned along with the laser from the Polytec VibroFlex focused on the resonator to measure its in-plane vibrations (section i). The actuators are driven via thermal voltage (V_{Th}), generated by DC source 1 (section ii). The curved beam is simultaneously actuated with an input controlled via a bias tee (section iii) that combines AC and DC signals, generated from the DC source 2 (section iv) and the Polytec VibroFlex Source (section v), respectively. Further, the Polytec VibroFlex Connect module (section vi), which interfaces with the sensor to collect data, outputting it into a graphical user interface (GUI) on a computer for analysis. The GUI displays data such as vibration amplitude and resonance characteristics. The system also includes Polytec VibroFlex Source connections for signal input and USB interface. The overall system is designed to monitor and analyze the resonator's dynamic response to various stimuli by combining advanced optical measurement, electronic control, and data visualization tools, comprehensively characterizing the MEMS device's performance.

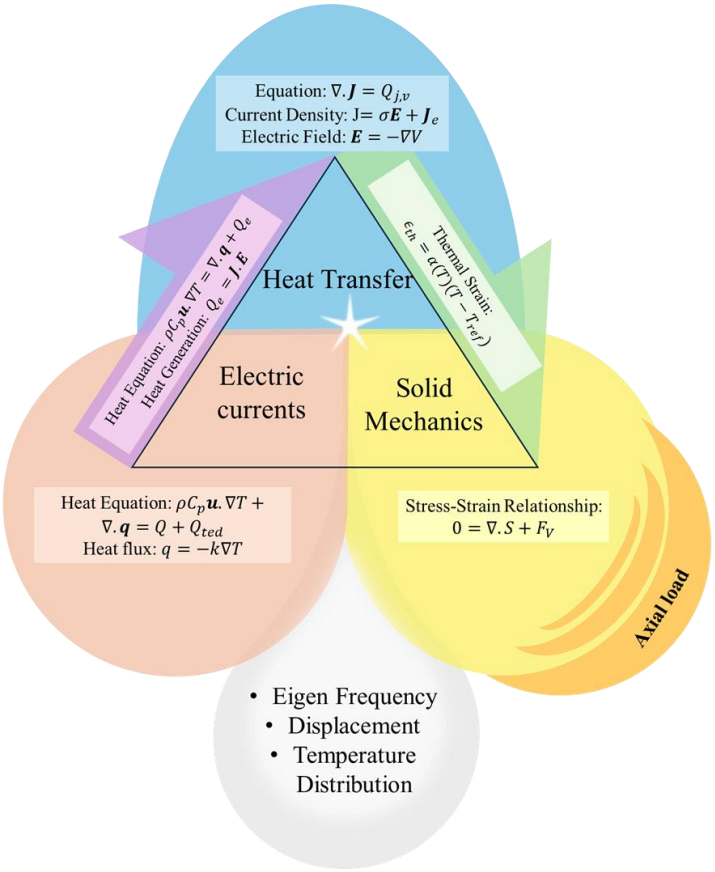

Fig.S4. Flowchart illustrating the simulation workflow that was performed using COMSOL

Supplementary Section 4: FEM Simulations and Analysis

The Multiphysics interaction governing the operation of the MEMS-based resonant magnetic microsensor is fundamentally described through the coupling of electric currents, heat transfer, and solid mechanics (Figure S4). The electric current flow within the device is dictated by the continuity equation $\nabla.J = Q_{j,v}$ where the current density J depends on the material conductivity σ and applied electric field E. The Joule heating effect, described by $Q_e = J.E$, serves as a source term in the heat transfer equations, leading to temperature variations governed by $\rho C_p u.\nabla T + \nabla.q = Q + Q_{ted}$, where the heat flux $q = -k\nabla T$ determines the spatial distribution of thermal energy. The resulting thermal expansion, expressed as $\epsilon_{th} = \alpha(T)(T - T_{ref})$, generates axial stress, influencing the solid mechanics response of the structure. The stress-strain relationship, given by $\nabla.S + F_V = 0$ governs the mechanical deformation, affecting the eigenfrequency shifts and displacement. This intricate coupling facilitates tunable magnetic field sensing by modulating the resonance frequency of the microbeam through the combined effects of thermally

induced axial stress and Lorentz force interaction.

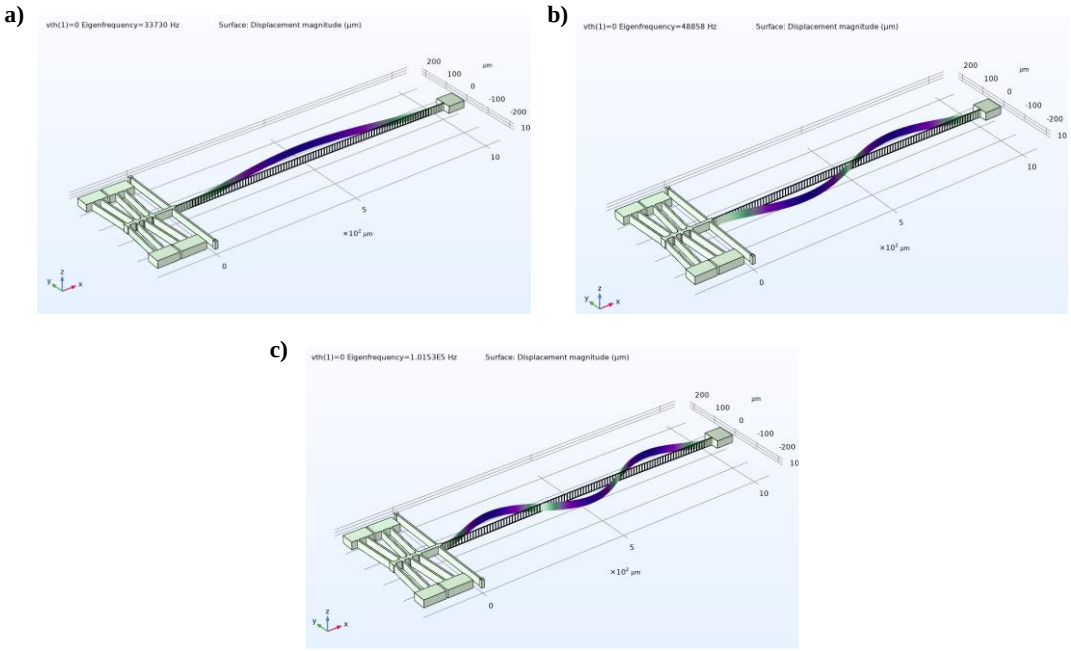

Fig. S5. The three eigen mode shapes of the curved microbeam resonator.

The finite element simulations shown in Figure S5 reveal the eigenmode shapes of the MEMS resonator, displaying its dynamic behavior under resonance. The first mode at 33.7 kHz exhibits a fundamental bending mode, where the microbeam undergoes symmetric in-plane oscillations with a single curvature along its length. The second mode, occurring at 48.8 kHz, represents a higher order bending mode, where the beam develops an additional nodal point, leading to an asymmetric deformation pattern. The third mode, observed at 101.5 kHz, corresponds to a complex multi-curvature deformation, introducing multiple nodal points along the beam. Understanding these mode shapes is essential for optimizing the resonator's performance, ensuring tunability, and enhancing its magnetic sensing efficiency through controlled axial loading and electrothermal actuation.

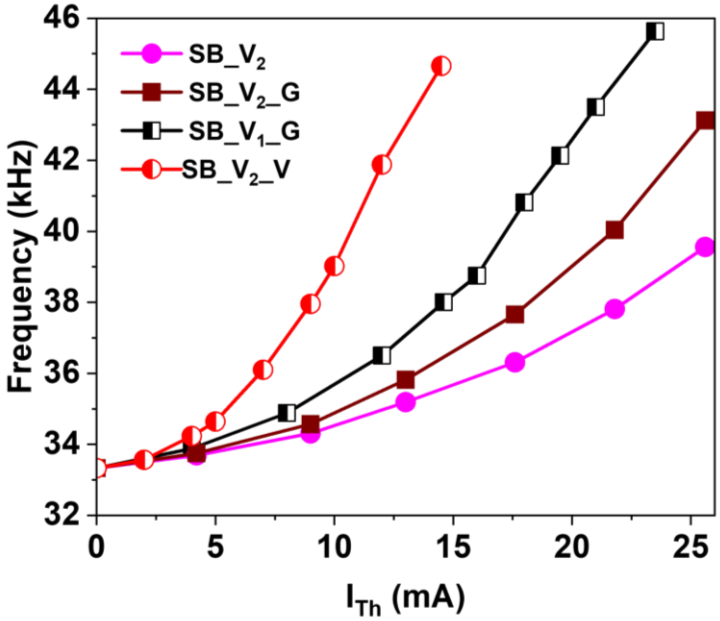

Fig. S6. Resonance frequency shift as a function of thermally induced current (I_{Th}) for different tuning cases (SB_V_1_G, SB_V_2, SB_V_2_G, and SB_V_2_V).

Supplementary Section 5: Additional Information

The different tuning configurations in table S2 define specific voltage and ground assignments to actuators, influencing the tunable arch beam stiffness and resonance frequency shifts. Case SB_V _V applies voltage to both the straight beam (SB) and V_1 actuator, introducing moderate axial stress and a balanced frequency shift. Case SBV_2 activates SB and V_2, causing a more pronounced frequency shift due to different stress distribution. Case SB_V_2 _G has a similar voltage assignment but modifies grounding, altering stiffness modulation. The SB_V_2_V case applies voltage to multiple actuators, leading to the highest axial stress, the most significant frequency shift, and enhanced sensitivity. A nonlinear frequency shift trend is present, where configurations involving more actuators (e.g., SB_V_2 _V) exhibit steeper frequency changes with

Table S2: Tuning configurations for the tunable arch beam, specifying voltage (V) and ground (GND) assignments for different electrodes.

Case	Tuning Parameters
Case *SB_V_1_G*	*A & E=V; B & F & G=GND*
Case *SB_V_2*	*C & E=V; D & G=GND*
Case *SB_V_2_G*	*C & E=V; F & G=GND*
Case *SB_V_2_V*	*C & E & G=V; D & F =GND*

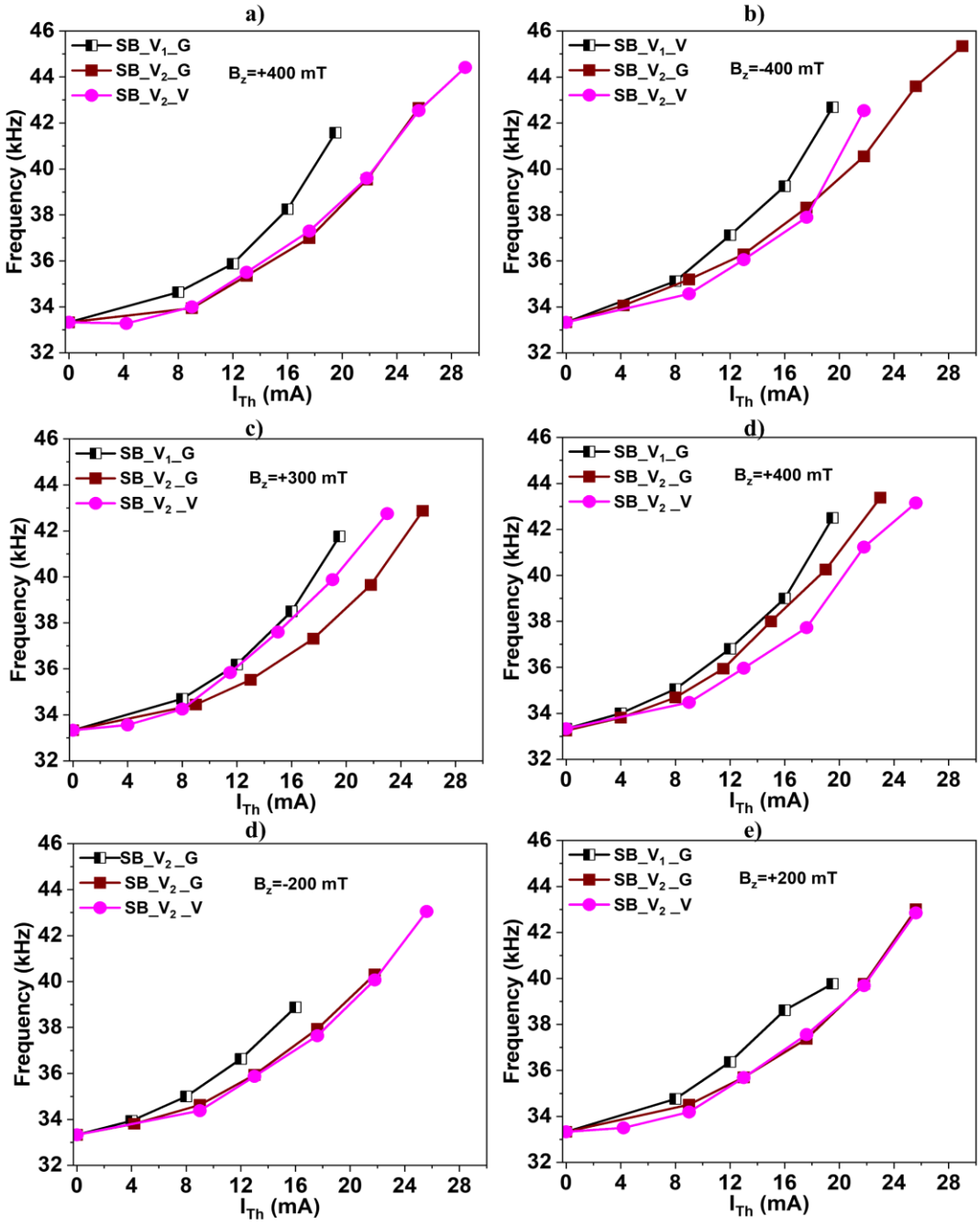

Fig. S7. Resonance frequency shift under varying magnetic field strengths a) 400 mT b) -400 mT c) 300 mT d) -300 mT e) 200 mT and f)-200 for different tuning cases.

increasing thermal voltage (Figure S6).

The graphs in Figure S7 illustrate the resonance frequency shift of the MEMS resonator under different tuning configurations and applied magnetic field strengths (B_z), ranging from -400 mT to +400 mT in a bidirectional out-of-plane orientation. The interaction between the thermally induced axial stress and the

Lorentz force modulates the resonator's stiffness, resulting in varying frequency responses. When a negative magnetic field (Bz = -400 mT, -300 mT, -200 mT) is applied, the Lorentz force aligns with the thermally induced compressive stress, leading to an increase in resonance frequency. This effect is most pronounced in configurations such as SBV_1G where the applied voltage enhances the axial load, causing a steeper frequency shift. Conversely, under a positive magnetic field (B_z = +200 mT, +300 mT, +400 mT), the Lorentz force opposes the thermally induced stress, resulting in lower frequency shifts compared to the zero-field condition. The magnitude of this effect depends on the tuning configuration. The nonlinear relationship between thermal current (I_{Th}) and resonance frequency further confirms that higher thermal excitation leads to stronger Lorentz force interactions, amplifying the sensitivity of specific tuning cases.

Supplementary Section 6: Sensitivity Calculations

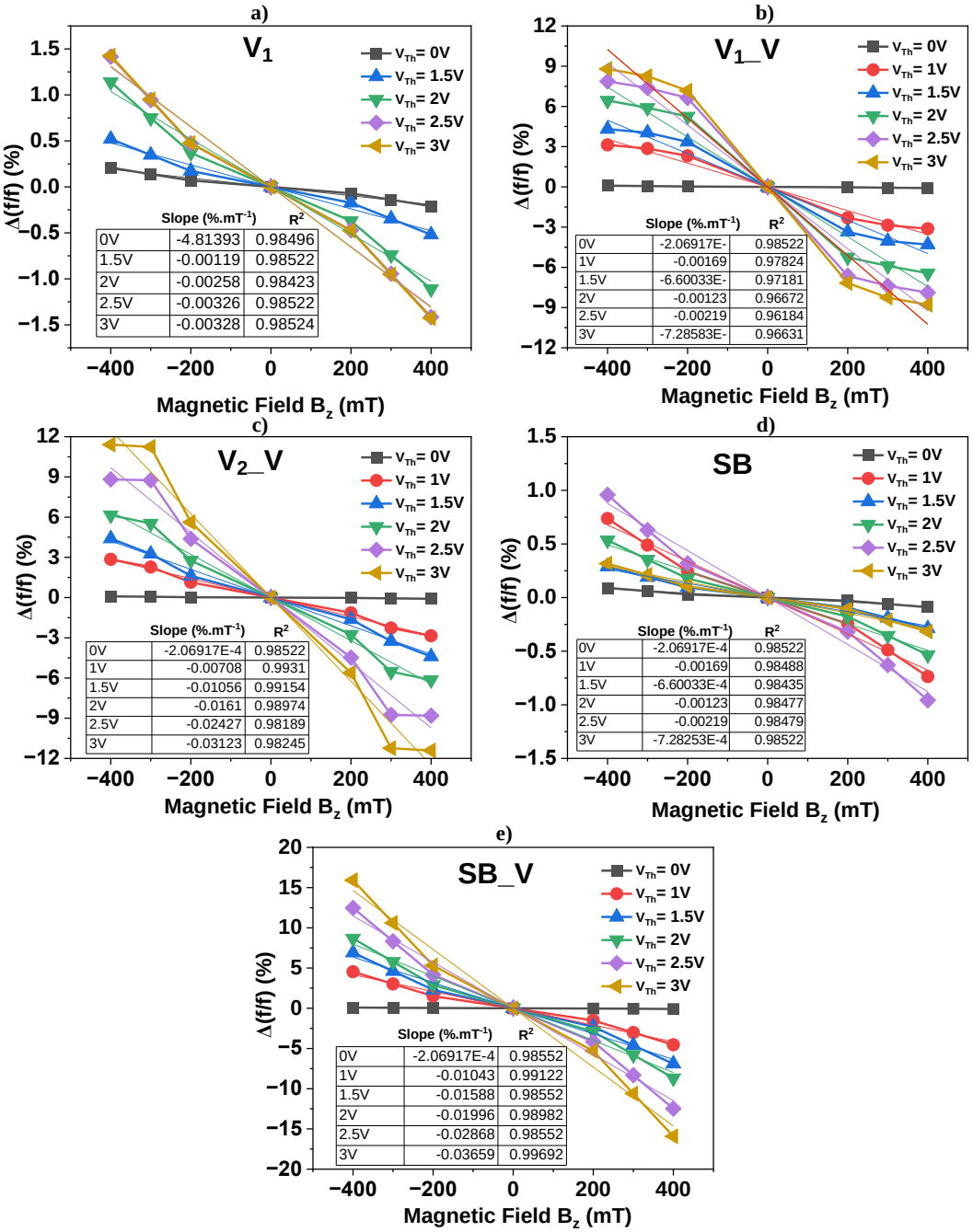

Figure S8 represents the individual sensitivity calculations of each tuning case at V_{Th} varying from 0-3V and external out-of-plane magnetic field B_z varying from -400 mT to +400 mT. The sensitivity for each case corresponds to the slope (linear fit) of %Δf/f vs B_z plots. Each slope value corresponds to a given V_{Th} or power range. The slope is given in $\%mT^{-1}$ for each case.

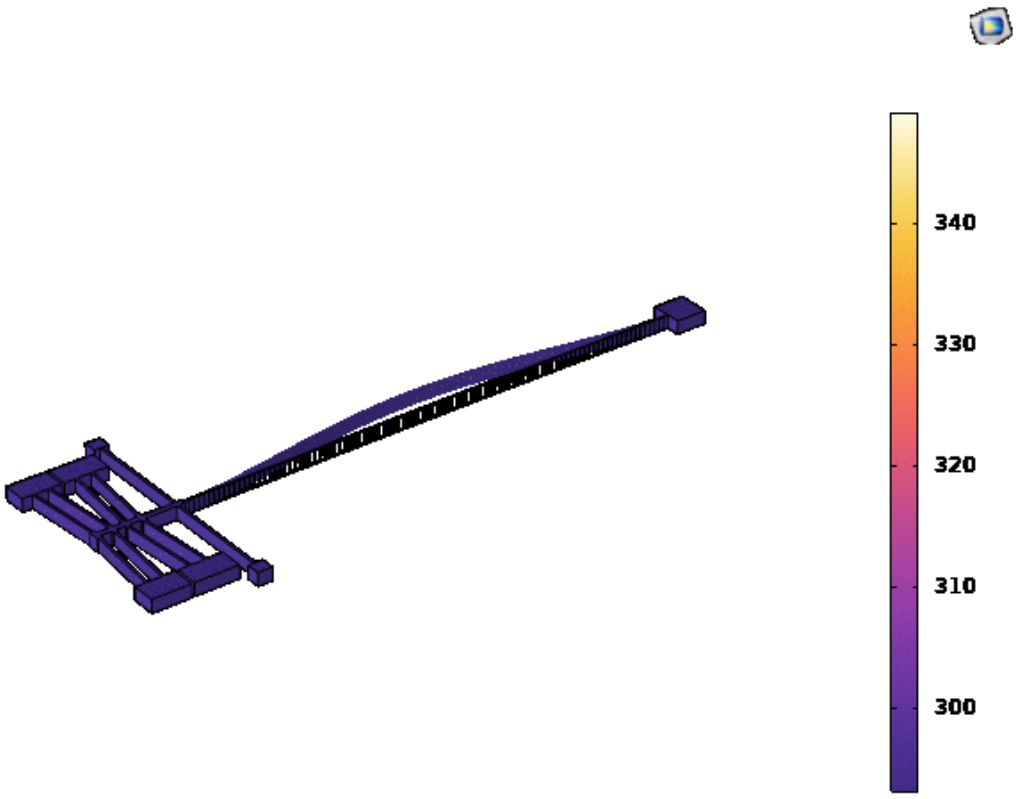

Fig. S9. Temperature distribution shown as an animation. The temperature variation occurs with varying $V_{Th.}$

Table S3: Parameters used for B_{min} calculations.

Parameter	**Value**
Mass(m)	1.80e-9 Kg
Frequency (f_1)	33KHz
Q-factor	60
Boltzmann Constant(k_b)	1.38e-23 J/K
Temperature (T)	300K
Damping coefficient (b)	0.0083

Table S4: B_{min} for all tuning cases.

Tuning Case	**B_{min} ($\mu T.Hz^{-1}$)**
V_1	3.91
V_1_V	0.9
V_2_V	0.9
SB	2.93
SB_V	0.83